Biofilms on Plastics Slow Photo-Oxidation while Promoting Surface Degradation

Goßmann, Isabel; Mitsutake, Hery; Degenhardt, Julius; Simonsen, Morten E; Liu, Fan

Published in:
Environmental Science & Technology

DOI (link to publication from Publisher):
10.1021/acs.est.5c08345

Publication date:
2025

Document Version
Publisher's PDF, also known as Version of record

Environmental Science & Technology

pubs.acs.org/est

Article

Biofilms on Plastics Slow Photo-Oxidation while Promoting Surface Degradation

Isabel Goßmann,* Hery Mitsutake, Julius Degenhardt, Morten E. Simonsen, and Fan Liu*

Cite This: *Environ. Sci. Technol.* 2025, 59, 22866−22873

Read Online

ACCESS | Metrics & More | Article Recommendations | Supporting Information

ABSTRACT: Plastics in natural environments undergo physicochemical aging, yet the role of biofilms—microbial communities that colonize plastic surfaces—remains poorly understood. To evaluate this, polyethylene terephthalate (PET) drinking bottles were exposed to natural freshwater to facilitate biofilm formation, and subsequently subjected to ultraviolet (UV) irradiation to assess the influence of biofilms on weathering. Results showed that biofilms exert dual roles, as both protectors and aggressors. When combined with UV exposure, biofilms intensified surface morphological alterations, root-mean-square roughness increased from ∼22 nm for pristine PET to ∼874 nm, and altered polymer crystallinity, as indicated by a shift in the Raman spectrum. They increased brittleness and reduced impact strength, facilitating UV to penetrate deeper layers and form cavities, thereby enhancing specific surface area from 2 g m^{-2} (pristine PET) to 22 g m^{-2}. In contrast, UV exposure alone induced extensive photo-oxidation, reflected in higher surface hydrophilicity and increased polar surface energy components. Biofilms may attenuate UV penetration but concurrently promote plastic fragmentation, which might indirectly favor additive leaching through mechanical weakening and structural degradation. These findings underscore the complexity of plastic weathering under natural conditions, which surpasses dynamics observed in laboratory studies on pristine materials.

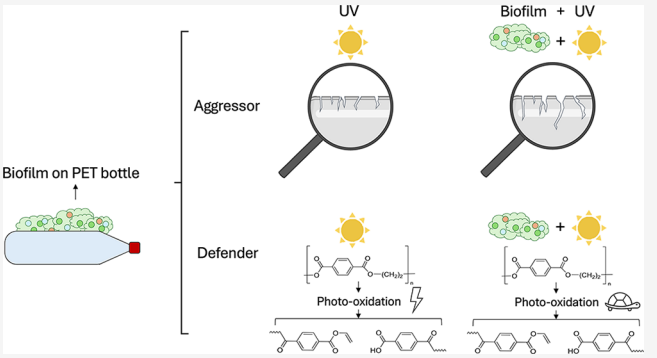

KEYWORDS: *plastic weathering, biofilm, biofouling, UV degradation, μ-Raman spectroscopy, atomic force microscopy, water contact angle, surface free energy, surface alteration*

1. INTRODUCTION

Environmental weathering significantly influences the long-term stability and ecological impact of plastics. Among various environmental factors, ultraviolet (UV) radiation and the rapid colonization of biofilms are the key players.[1] It is well-known that UV radiation induces oxidative degradation, increasing surface roughness and promoting fragmentation through the formation of oxygen-containing functional groups.[2−4] The impact of biofilms on plastic weathering, however, is rarely studied.

Biofilms are structured microbial communities embedded in a self-produced extracellular matrix, primarily composed of polysaccharides, proteins, and nucleic acids.[5] They readily form on natural and synthetic surfaces across diverse ecosystems, from rocks and soils to biomedical and industrial settings (e.g., implants, pipelines, water treatment systems).[6,7] On plastics, biofilm may act as a protective layer against for instance, UV radiation, thus delaying plastic degradation. Also, they may influence the physiochemical properties of plastic surface and mediate the release of additives. Furthermore, biofilms could act as a potential driver, promoting microbial interactions that could alter the polymer's chemical structure.[8,9] Despite these potential effects, biofilms are rarely considered when assessing the stability of plastics exposed to the environment, leaving a major gap in our understanding of plastic weathering.

Polyethylene terephthalate (PET) drinking bottles exemplify this problem. According to the United Nations Environment Programme, PET bottles are the second most prevalent single-use plastic waste worldwide, after cigarette butts.[10] Once released into the environment, PET provides extensive surface area for biofilm formation and is readily exposed to sunlight. Its transparency also makes it particularly amenable to high-resolution surface and chemical analyses. This study addresses the knowledge gap by testing how biofilm growth influences the UV-driven degradation of PET. We compare pristine and biofilm-colonized PET exposed to controlled UV aging and examine the resulting changes in surface morphology, surface energy and chemical structure. To capture these changes, we employed a combination of high-resolution Atomic Force

Received: June 23, 2025
Revised: October 5, 2025
Accepted: October 7, 2025
Published: October 15, 2025

Microscopy (AFM), μ-Raman spectroscopy, and contact-angle measurements.

By integrating these complementary approaches, we evaluate whether biofilms primarily act as protective barriers that slow for example photo-oxidation or, conversely, as agents that accelerate polymer degradation under environmental stress. Our results provide new insight into the role of biofilms in plastic weathering and inform future assessments of the environmental fate and impacts of plastic debris.

2. METHODS

2.1. Sample Preparation: Pristine and Biofilm-Colonized Material. Pristine PET drinking water bottles, hereinafter referred to as PET, were cut into pieces (3 × 3 cm and 8 × 3 cm), placed in Petri dishes, and covered with aluminum foil to prevent UV exposure, labeled as PET_P. Additionally, PET was submerged approximately 15 cm below the water surface of a local stormwater retention basin in a custom-built cage at the end of July 2024. After two months of environmental exposure, the PET was retrieved, by which time a biofilm had formed on the exposed surfaces. The biofilm-colonized PET was then cut into pieces (3 × 3 cm and 3 × 8 cm), stored in Petri dishes, and again covered with aluminum foil. These samples are labeled PET_WB. Pictures of the custom-built cage, its deployment, and biofilm growth are displayed in the Supporting Information (SI, Figures S1 and S2).

2.2. Accelerated Weathering. For accelerated weathering, both PET_P and PET_WB were exposed to UV−C irradiation in a BS-02 chamber (Opsytech Dr. Gröbel GmbH, Germany), equipped with eight UV−C lamps (253 nm, 10 mW cm^{-2}). The solar equivalence was calculated following Simon et al.,[11] by comparing the total photon output from the UV−C lamps with the estimated yearly average photon exposure in Denmark. For a more detailed calculation refer to the SI (Text Section S2). Based on the number of emitted photons, samples were exposed to UV−C irradiation for 7 days per side, equivalent to 25 days of natural sunlight exposure. The weathered PET pieces were stored in Petri dished covered in aluminum foil. UV-treated samples are hereinafter labeled as PET_P_UV and PET_WB_UV, respectively. We note that the use of UV−C constitutes a limitation, as it does not reflect the environmentally relevant UV spectrum (UV-A/B). Furthermore, only a single exposure duration of 25 days was evaluated, as this experiment was designed as an exploratory study to determine whether biofilm-mediated weathering produces measurable effects.

2.3. AFM Topography. Surface topography of PET samples was characterized by AFM, which scans the surface with a nanoscale cantilever tip to quantify morphology at nanometer resolution.[12,13] AFM is well suited for detecting environmentally induced changes in plastic surfaces.[3]

Prior to AFM topography measurements, biofilms were carefully removed from PET_WB and PET_WB_UV samples under running water. Gentle manual cleaning was applied when necessary to ensure complete removal. Measurements were conducted with a scanning probe microscope (SPM) (OmegaScope) integrated with a μ-Raman system (Horiba Scientific). Data acquisition and processing were performed using AIST software (version 3.5.163). For AFM topography measurements, SPM probes from MikroMasch were used, specifically the HQ:NSC14/Al BS model, which consists of a standard AFM probe with a pyramidal silicon tip, a beam-type silicon cantilever, and a rectangular silicon chip. Measurements were conducted in AC mode (semicontact AFM mode) using a QScan at a scanning rate of 1.0 Hz over an area of 10 × 10 μm, with a resolution of 512 × 512 pixels. Each PET condition was measured in triplicate on distinct subareas selected along a diagonal across the sample surface to include both edge and central regions.

Initial data processing was performed using the IApro tool within the AIST software suite. A plane-level filter was applied, and the minimum z-value was normalized to zero nm. Subsequent data analysis was carried out using Python (Version 3.12) within the Spyder (IDE 5.5.1) integrated development environment. Statistical analysis of AFM data employed a one-way analysis of variance (ANOVA), followed by Tukey's honestly significant difference (Tukey's HSD) posthoc test to identify significant differences among the conditions, as described by Schefer et al.[3] The significance level was set as $p = 0.05$. Additionally, root-mean-square roughness (RMS) and specific surface area (SSA) were calculated following the method proposed by Schefer et al.[3]

2.4. 3D Mapping with μ-Raman Spectroscopy. Chemical changes in the PET surface were analyzed using μ-Raman spectroscopy, which provides spatially resolved vibrational fingerprints of polymer functional groups and enables micrometer-scale chemical imaging.[14−17]

To facilitate a comprehensive analysis of surface chemistry and in-depth heterogeneity, 3D mapping was conducted using μ-Raman spectroscopy (XploRA Plus, Horiba Scientific), utilizing the LabSpec 6.7.2 software. PET samples from all experimental conditions (PET_P, PET_WB, PET_P_UV, and PET_WB_UV), with biofilm removed prior to analysis, were subjected to 3D mapping. The mapped area spanned 40 × 40 μm in the x- and y-plane. Along the z-axis, the motorized XYZ stage traversed 100 μm vertically, resulting in a total analyzed volume of 160,000 μm^3. The lateral and vertical step sizes were 2.2 and 16.7 μm, respectively. Measurements were conducted in triplicate by analyzing three distinct subareas per sample. Samples were exposed to a laser excitation of 785 nm (28 mW nominal laser power), dispersed by a 600 lines mm^{-1} diffraction grating onto a charge-couple device (CCD) detector. A 50× long-working-distance objective (N.A = 0.50) was used, covering a spectral range of 775−2000 cm^{-1}. This configuration gives a theoretical lateral spatial resolution of 958 nm and 6.3 μm of depth of focus.[18] All spectral data acquired for the 3D maps were exported as ASCII format and subsequently processed in MATLAB v. 24.2 (The Mathworks Inc., Natick, MA). The baseline was corrected by rubber band correction.

2.5. Contact Angle Measurements and Surface Free Energy (γ_s) Calculation. Wettability and surface free energy (γ_s) were determined from water and diiodomethane contact angles to calculate polar (γ_s^P) and dispersive (γ_s^D) components.[19−21] These measurements indicate surface chemical modifications relevant to polymer−environment interactions.[22]

Static contact angle measurements were performed using a Krüss DSA100 with an automated dispensing unit. Droplets of ultrapure water (5 μL) and DIM (2 μL) were deposited onto the surface under ambient laboratory conditions. To ensure reproducibility and statistical validity, five independent replicates were conducted per sample, with each replicate comprising five individual contact angle measurements. γ_s was calculated using combination of Good's and Young's equation derived by Owens and Wendt and Fowkes,[19,21] which involves

https://doi.org/10.1021/acs.est.5c08345
Environ. Sci. Technol. 2025, 59, 22866−22873

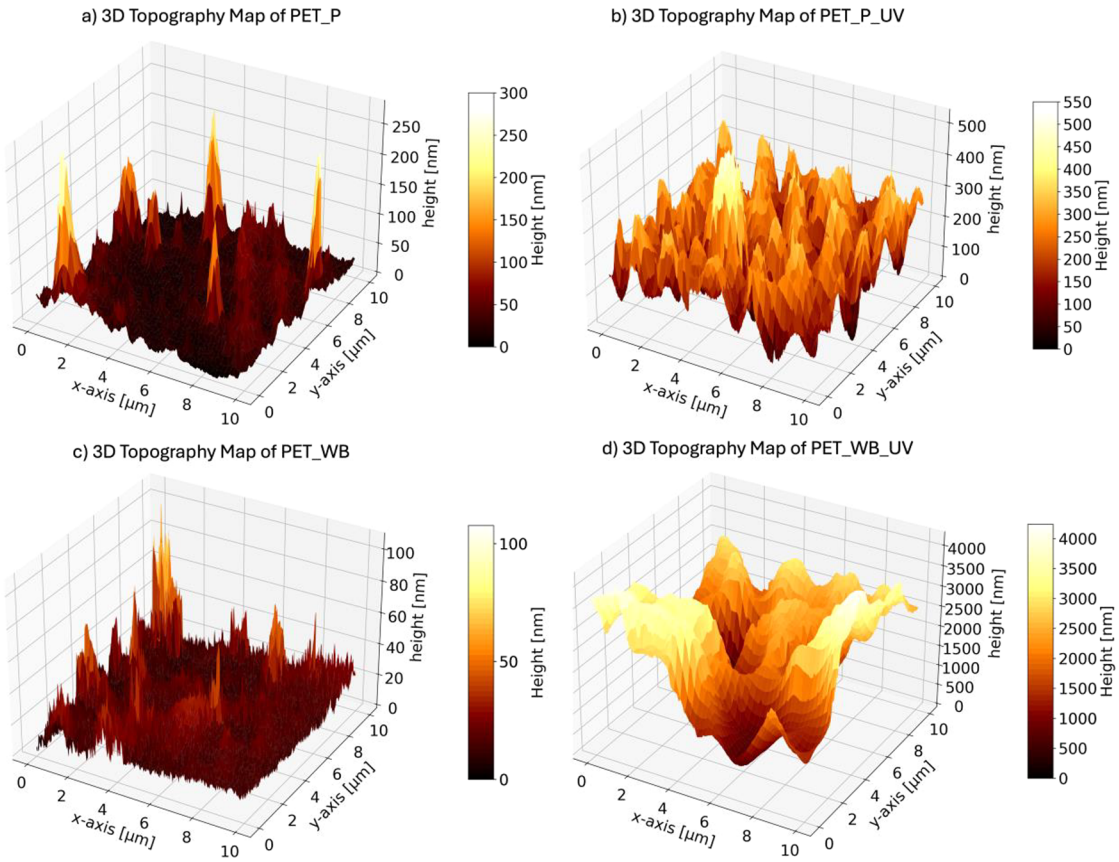

Figure 1. 3D Topography maps of PET surface under four conditions: (a) pristine PET (PET_P), (b) UV-aged pristine PET (PET_P_UV), (c) biofilm-colonized PET (PET_WB), and (d) UV-aged PET after biofilm colonization (PET_WB_UV). The *x*- and *y*-axes represent lateral dimensions in μm, and the *z*-axis indicates surface height in nm. Each map corresponds to the first of three replicate measurements.

contact angle data from both a polar and a nonpolar liquid in conjunction with their known surface tension components. Surface tension values for water and DIM were obtained from the instrument manufacturer's application note (AN213/CR). For water, a total surface tension of 72.8 mN m^{-1} was used, with γ_s^D and γ_s^P components of 26.4 and 46.4 mN m^{-1}, respectively. For DIM, a total surface tension of 50.8 mN m^{-1} was assumed, consisting entirely of γ_s^D. The γ_s^P and γ_s^D. contributions to γ_s of each sample were determined for each replicate by solving the Owens-Wendt equations, and the results were averaged. Detailed calculations are given in the SI (Text Section S3).

3. RESULTS AND DISCUSSION

3.1. General Observations. Initially transparent, PET_P became opaque upon UV exposure. After two months in the pond, a thin layer of biofilm (~1 mm) covered the entire PET surface. Following gentle removal of the biofilm, most of PET_WB remained transparent, but opaque spots persisted, likely indicating areas of pronounced biofilm-induced surface alteration. Similar to PET_P, PET_WB became completely opaque after UV aging. Pictures of the different PET conditions and the biofilm growth are shown in the SI (Figures S2 and S4). Details of the biofilm's microbial community composition, obtained by DNA extraction, 16S rRNA gene amplification, sequencing and subsequent sequence-data processing following the pipeline described by Degenhardt et al.,[23] are provided in the SI (Text Section S1).

3.2. AFM Topography. The AFM topography analysis revealed notable alterations in the PET surface. Figure 1 presents 3D topography maps of PET surfaces following biofilm colonization and/or UV aging. All measurements were performed in triplicate; Figure 1 shows one representative scan from each condition, and the description refers to this replicate. PET_P exhibited surface height variations ranging from 0 to 270 nm (Figure 1a). Biofilm formation appeared to smooth the surface (Figure 1c), reducing height variation to 0−100 nm. In contrast, UV aging slightly increased the surface roughness of pristine plastic, with height variation extending up to 540 nm (Figure 1b). Notably, biofilm growth followed by UV aging resulted a drastically roughened surface, characterized by localized cavity formation, with height variations spanning from 0 to 4000 nm (Figure 1d). Corresponding 2D contour plots for all four conditions, as well as 3D topography maps of the additional triplicate scans, are provided in the SI (Figures S5−S16, respectively).

These morphological changes were further supported by RMS and SSA analysis (Figure 2), based on triplicate measurements for each condition. RMS values for PET_P ranged from 14.5 to 27.3 nm, whereas PET_WB exhibited lower values (4.3−8.4 nm). UV aging of pristine plastic increased the RMS to 71.6−81.6 nm, while the combined effects of biofilm growth and UV aging led to a substantial increase, with RMS reaching 741.5−964.5 nm (Figure 2a). According to Tukey's HSD posthoc test, PET_WB_UV differed significantly from all other conditions, whereas PET_P, PET_P_UV, and PET_WB showed no significant

https://doi.org/10.1021/acs.est.5c08345
Environ. Sci. Technol. 2025, 59, 22866−22873

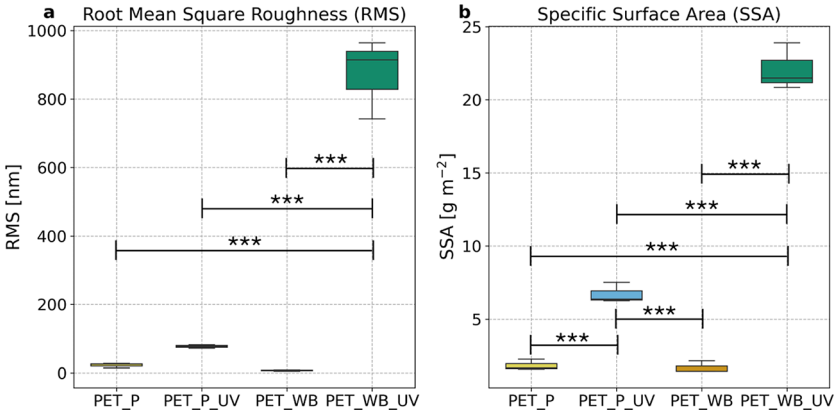

Figure 2. Comparison of four PET conditions in (a) root-mean-square roughness (RMS, nm), and (b) specific surface area (SSA, g m^{-2}) for pristine PET (PET_P), UV-aged pristine PET (PET_P_UV), biofilm-colonized PET (PET_WB), and UV-aged PET with biofilm colonization (PET_WB_UV). The central line within each box is the median value. Box limits define the upper and lower quartiles (Q3 and Q1), describing the interquartile range (IQR). Whiskers extend from the box to 1.5× IQR. Statistical significance is indicated as follows: p-value < 0.001 "***", < 0.01 "**", and <0.05 "*".

differences. For SSA (Figure 2b), all conditions exhibited significant differences, except for PET_P and PET_WB.

When these results are compared with previous studies analyzing surface changes after UV aging using AFM, certain parallels emerge. Schefer et al.,[3] who employed a similar UV exposure duration (28 days vs 25 days here), reported an increase in RMS following UV aging, aligning with the findings of this study. However, while the RMS increase from PET_P to PET_P_UV was noticeable in the present study, it was not statistically significant, in contrast to the significant changes documented by Schefer et al.[3] Conversely, their study reported an almost unchanged SSA after UV aging, whereas the present study shows significant SSA differences between PET_P and PET_P_UV. To our knowledge, no previous studies have incorporated biofilm exposure in this context, precluding direct comparison. RMS values of PET_WB decreased relative to PET_P, while SSA remained largely unchanged. Despite biofilm removal prior to analysis, residual thin layers may have remained, potentially filling surface irregularities and thereby contributing to the reduction in RMS. Possible surface damage through the manual biofilm removal was unlikely, since 3D surface plots of PET_WB appear visibly rough and irregular with sharp peaks (SI, Figure S7).

Upon UV irradiation, PET_WB_UV exhibited significant alterations in both RMS and SSA compared to all other conditions (PET_P, PET_P_UV, and PET_WB). AFM topography further revealed localized cavity formation on the surface of PET_WB_UV. The 0−4000 nm height range and the significant differences in RMS and SSA are primarily attributed to this cavity formation, with a likely contribution from differential swelling/shrinkage associated with the hydrated biofilm matrix. Biofilms are highly hydrated and retain water, creating moist microenvironments that can dry nonuniformly after the transition from the aqueous biofilm phase to the UV exposure in air.[5] Such nonuniform drying is known to generate mismatch stresses in polymer films, which can drive defect formation, and thus help open or enlarge cavities.[24] These findings indicate that biofilm, when combined with UV exposure, functions not as a passive protective barrier but as an active contributor to substantial surface modification.

3.3. μ-Raman Spectroscopy. *3.3.1. Laser Attenuation in z-Direction.* Laser attenuation along the z-direction is illustrated in the SI (Figures S9 and S10), where the spectral range between 1097 and 1120 cm^{-1} is highlighted. A decrease in intensity is observed for the PET_P sample (Figures S9a−c and S10a−c), and four distinct layers can be identified, indicating laser penetration and subsequent attenuation within the material. A similar pattern is observed in the first replicate of PET_WB (Figures S9g and S10g). In contrast, the third replicate (Figures S9i and S10i) exhibits only two distinguishable layers, while the second replicate (Figures S9h and S10h) shows no clear layer separation. This trend persists across all samples subjected to UV aging (Figures S9d−f, j−l and S10d−f, j−l), suggesting that UV exposure alters material's optical properties, thereby reducing laser penetration compared to pristine samples. While this effect is more apparent after UV aging − likely due to increased opacity − changes are also visible after biofilm formation on PET_WB. These alterations hinder direct comparisons of signal intensity along the z-axis without applying correction methods, such as the Monte Carlo Multi-Layered (MCML) model.[25] Although a more detailed analysis could yield further insights, it falls beyond the scope of the present study. Accordingly, the x-axis in Figures 3 and 4 represents the displacement of the microscope stage along the z-direction.

3.3.2. Comparison of Raman 3D Maps. Recently,[26] introduced a high-resolution 2D Raman mapping method to analyze structural anisotropies, including crystallinity and molecular alignment, in different PET materials. Their study focused on characteristic Raman bands reflective of the structural state of PET. The peak at 1097 cm^{-1} (ring C−C, ester C(O)−O, ethylene glycol C−C stretching (trans confirmation)) intensifies with increasing crystallinity, whereas the 1120 cm^{-1} band (ring C−H in-plane bending, ester C(O)−O and ethylene glycol C−C stretching (gauche confirmation)) is more prominent in amorphous regions. The intensity ratio of these bands provides a direct indicator of PET crystallinity.

Based on these findings, attention was given to the Raman peaks at 1097 and 1120 cm^{-1}. Figure 3 presents a plot of the ratio of their peak heights for the four PET conditions and the seven z-positions. More detailed box plots showing the median, data distribution, and outliers are provided in the SI (Figure S20). In one of the maps obtained from

https://doi.org/10.1021/acs.est.5c08345
Environ. Sci. Technol. 2025, 59, 22866−22873

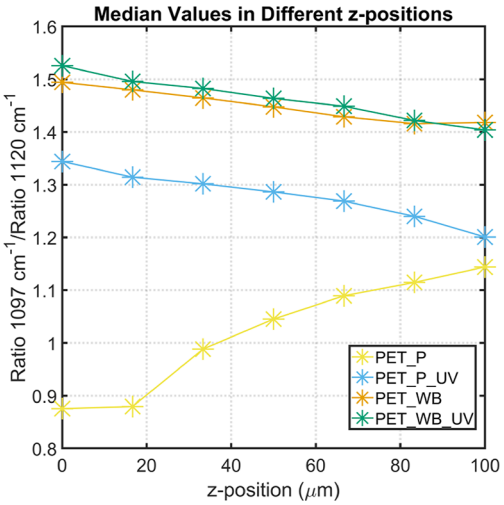

Figure 3. Plot of the median values of the peak height ratio between 1097 and 1120 cm^{-1} for pristine PET (PET_P, yellow), UV-aged pristine PET (PET_P_UV, blue), biofilm-colonized PET (PET_WB, orange), and UV-aged PET after biofilm colonization (PET_WB_UV, green), measured from the surface (0 μm) to a depth of 100 μm in triplicate.

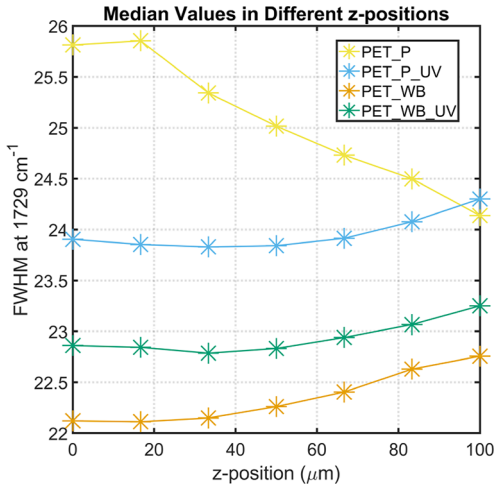

Figure 4. Plot of the median values of the full width at half-maximum (FWHM) at 1729 cm^{-1} for pristine PET (PET_P, yellow), UV-aged pristine PET (PET_P_UV, blue), biofilm-colonized PET (PET_WB, orange), and UV-aged PET after biofilm colonization (PET_WB_UV, green), measured from the surface (0 μm) to 100 μm in depth, based on triplicate measurements.

PET_WB_UV, some spectra showed a very intense fluorescent background caused by biofilm residues; these spectra were considered outliers and excluded from the analysis. For PET_P_UV, PET_WB, and PET_WB_UV, the 1097 cm^{-1} peak consistently exceeded that at 1120 cm^{-1} across all z-positions, yielding a ratio >1. In contrast, PET_P initially exhibited a ratio below 1 − indicating a higher relative intensity at 1120 cm^{-1} - up to a depth of approximately 33 μm, after which the ratio exceeded 1. At around 83 μm, the ratios of PET_P and PET_P_UV converged, suggesting structural differences diminished. A Kruskal−Wallis test followed by Dunn's posthoc pairwise comparison confirmed these significant differences between sample groups up to the depth of 83 μm. Beyond this depth, no significant differences were detected. Biofilm-exposed PET materials (PET_WB and PET_WB_UV) maintained structural consistency from the surface down to the penultimate layer (z-position: 83 μm), significantly distinct from the nonbiofilm-exposed samples (PET_P and PET_P_UV).

These findings reveal that PET_P, initially characterized by a predominance of gauche conformation and a more amorphous structure, undergoes a transition toward trans conformation − indicative of increased crystallinity − upon exposure to UV radiation and/or biofilm colonization. The most pronounced shift toward this crystalline configuration occurs when both UV radiation and biofilm are present, although biofilm alone induces a comparable transformation. In contrast, UV exposure alone results in the least structural change. These findings indicate that biofilm exerts a stronger influence on the structural state of the ethylene glycol segment in PET than UV radiation. Furthermore, the UV-induced changes from amorphous to crystalline are most predominantly confined at the surface, whereas biofilm-induced changes extend consistently throughout the depth profile (up to 100 μm), indicating that biofilm-induced alterations are not limited to the surface but penetrate into the bulk material.

Additionally, Perret et al.[16,26] focused on the 1729 cm^{-1} (C═O stretching) band, which narrows with increasing crystallinity, also reflecting changes in chain packing density. For differentiating the peak shape at 1729 cm^{-1}, the full width at half-maximum (FWHM$_{1729}$) was calculated and compared. Lower FWHM$_{1729}$ indicate sharper peaks and are typically associated with higher density and greater crystallinity in polymer structures, whereas higher values suggest reduced density and a more amorphous character.[16,26] Figure 4 the FWHM$_{1729}$ values plotted across the z-positions. Mor detailed box plots illustrating the median, data distribution, and outliers, are provided in the SI (Figure S21). PET samples exposed to UV and biofilm exhibited sharper peaks at 1729 cm^{-1} compared to pristine PET. Furthermore, the lowest FWHM$_{1729}$ (sharpest peak) was found for PET_WB, followed by PET_WB_UV, and finally PET_UV. This aligns with the previously discussed 1097/1120 cm^{-1} band ratio, supporting the transition from an amorphous structure in PET_P to more crystalline structures in PET_P_UV, PET_WB, and PET_WB_UV.

Given that amorphous regions generally exhibit lower density than crystalline ones,[27] the observed decrease in FWHM$_{1729}$ across treated samples suggests that both biofilm formation and UV radiation contributed to an increase in PET density. Again, structural changes extended to a depth of 100 μm in biofilm-exposed samples, whereas UV radiation alone affected only the top 50 μm.

However, the Kruskal−Wallis test followed by Dunn's posthoc analysis for pairwise comparisons, revealed significant differences between all four PET conditions at each z-position, except at 83 μm between PET_P and PET_P_UV (p = 0.0514). This further supports the interpretation that biofilm-induced transformations are more profound and persistent in deeper layers than those caused by UV alone. However, as this study utilized UV−C light, it is important to note that longer-wavelength UV−A and UV−B radiation may penetrate deeper into the material and potentially induce changes at greater depths.

Overall, a synergistic effect between biofilm formation and UV exposure on PET crystallization is indicated. As shown in Figure 1, the combined treatment increases surface-height variation and leads to localized cavity formation (Figure 1d),

https://doi.org/10.1021/acs.est.5c08345
Environ. Sci. Technol. 2025, 59, 22866−22873

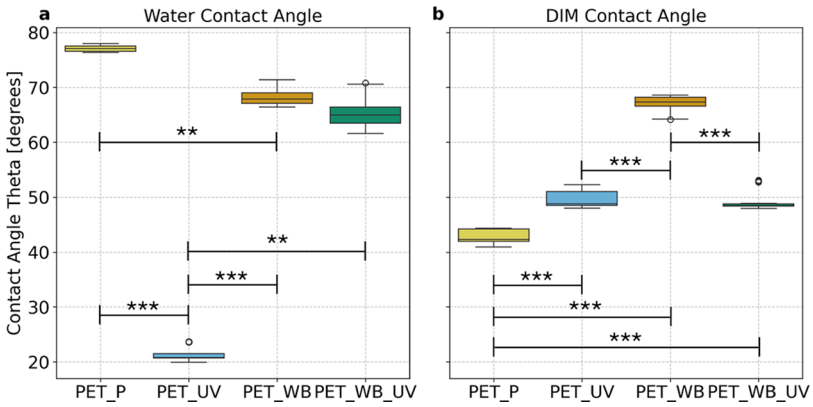

Figure 5. Contact angle measurements for water (a) and diiodomethane (DIM, (b) for four PET conditions: pristine PET (PET_P), UV aged pristine PET (PET_P_UV), biofilm-colonized PET (PET_WB), and UV aged PET after biofilm colonization (PET_WB_UV). The central line within each box is the median value. Box limits define the upper and lower quartiles (Q3 and Q1), describing the interquartile range (IQR). Whiskers extend from the box to 1.5 × IQR. Statistical significance is indicated as follows: p-value < 0.001 "***", < 0.01 "**", and <0.05 "*".

which exposes subsurface PET to environmental conditions. Microbial exudates such as sugars and carboxylic acids[28] can act as chemical nucleation agents that promote crystal growth;[29,30] consistent with this, Legras et al.[29] reported that salts of carboxylic acids react with PET ester bonds and promote crystallization. The Raman carbonyl band at 1729 cm^{-1} and its $FWHM_{1729}$ (Figure 4) differ between biofilm/UV-treated and pristine PET, supporting changes in surface chemistry and crystallinity.

3.4. Contact Angle Measurements and Surface Free Energy (γ_s). Water contact angles ranged from an average of 21.3° on PET_UV to 77.1° on PET_P, with intermediate values observed for PET_WB (68.2°) and PET_WB_UV (65.3°), indicating increased hydrophilicity upon surface modification − most pronounced after UV treatment alone (Figure 5a). In contrast, DIM contact angles displayed a different pattern: highest on PET_WB (67.0°), followed by PET_UV (49.7°), PET_WB_UV (49.3°), and lowest on PET_P (42.8°) (Figure 5b). Statistical analysis using the Kruskal−Wallis test confirmed that these significant differences in contact angles for both water and DIM. Dunn's posthoc test with Bonferroni correction revealed all pairwise differences in water contact angles were statistically significant, except between PET_WB and PET_WB_UV. For DIM contact angles, all comparisons were statistically different except between PET_UV and PET_WB_UV. These findings align with Schefer et al.,[3] who reported significantly lower water contact angles, and hence greater hydrophilicity for UV-aged PET compared to pristine samples.

Calculations of γ_s revealed clear differences among the four PET conditions (Figure 6). PET_P exhibited a γ_s of 41.7 mN m^{-1}, dominated by γ_s^D (38.1 mN m^{-1}) and minimal γ_s^P (3.5 mN m^{-1}), indicating a predominately apolar surface. PET_WB showed the lowest γ_s (37.4 mN m^{-1}), characterized by a reduced γ_s^D and a moderately increased γ_s^P. This suggests that biofilm exposure alone alters the surface chemistry without enhancing overall surface energy, and, in fact, reduces chemical surface activity compared to PET_P. In contrast, PET_UV showed the highest γ_s (69.2 mN m^{-1}), with comparable contributions from γ_s^P and γ_s^D, indicating significant polar functionalization and enhanced surface chemical activation following UV treatment. The combined treatment (PET_WB_UV) resulted in an intermediate γ_s (44.5 mN m^{-1}), driven by an γ_s^P increase compared to PET_P.

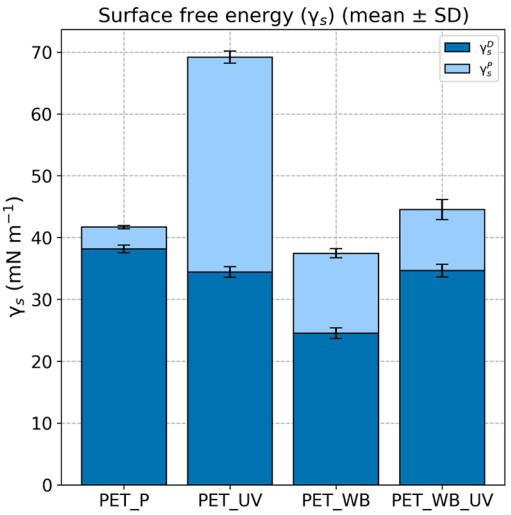

Figure 6. Surface free energy (γ_s) with its components: dispersive (γ_s^D, dark blue) and polar (γ_s^P, light blue) for the four PET conditions: pristine PET (PET_P), UV-aged pristine PET (PET_P_UV), biofilm colonized PET (PET_WB), and UV-aged PET after biofilm colonization(PET_WB_UV). Bars represent the mean of replicate measurements; error bars indicate standard deviation (SD) of the corresponding component.

Statistical analysis confirmed that all treatment conditions led to significant differences in γ_s and its components. While most pairwise comparisons showed statistically significant differences in γ_s, but also in γ_s^D and γ_s^P. The only exception was between PET_UV and PET_WB_UV, where γ_s^D did not differ significantly. Statistical results from Tukey's HSD posthoc test are displayed in the SI (Tables S2−S4).

A study by Gewert et al.[22] investigated the degradation pathways of PET and demonstrated that UV radiation cleaves ester bonds, resulting in the formation of carboxylic acid (highly polar) and vinyl end groups, either directly or via radical intermediates. This photo-oxidative process likely explains the pronounced increase in wettability and hydrophilicity observed in PET_UV, along with the substantial rise in γ_s, approximately 50% of which is attributed to γ_s^P. PET_WB_UV exhibited a similar trend, though the changes were less pronounced. In the absence of UV radiation, PET_WB did not show an overall increase in γ_s, though an

https://doi.org/10.1021/acs.est.5c08345
Environ. Sci. Technol. 2025, 59, 22866−22873

increase in its γ_s^P was observed. Zhang et al.[31] reported minimal microbial or lipase-induced degradation of PET, hence biofilm was unlikely the primary cause for these changes. However, given that biofilm-exposed samples were submerged in a local stormwater retention basin, hydrolytic degradation is a more plausible contributor to the elevated γ_s^P in PET_WB relative to PET_P. Gewert et al.[22] noted that hydrolysis induces a degradation pathway similar to photo-oxidation, resulting a formation of carboxylic acid and alcohol groups, albeit at a slower rate.

The statistically significant differences between PET_WB and PET_WB_UV indicate that UV-induced surface chemistry changes beyond the effects of hydrolysis. These findings suggest that while the biofilm offered partial protection, it was insufficient to fully shield the PET surface from UV-induced transformations. While these changes were reflected in γ_s measurements, these structural conversion − from ester to carboxyl groups − likely remained undetectable by μ-Raman spectroscopy, as the vibrational frequencies of the respective functional groups are too similar to be distinguished.[32]

3.5. Environmental Implications. This study demonstrates that both UV radiation and biofilm colonization significantly influence the degradation pathways of PET under environmentally relevant conditions. While UV radiation alone primarily induces surface-level structural changes, biofilm colonization promotes more profound chemical and morphological alterations deeper into the material, increasing polymer brittleness and crystallinity. Notably, when biofilm formation precedes UV exposure, degradation is markedly intensified, characterized by pronounced changes in surface roughness, cavity formation, and increased surface area. These alterations are likely to enhance the material's susceptibility to fragmentation[33] and may facilitate the release of embedded additives, with potential implications for nano- and microplastic generation and pollutant dispersion in aquatic systems. The results also highlight a more complex role of biofilms than previously recognized. Although biofilms were initially hypothesized to act as a protective layer on plastic surfaces, our findings show that this effect is property-dependent. For instance, UV exposure had a stronger effect on surface hydrophilicity and surface free energy than biofilm colonization alone. In this context, biofilms appeared to attenuate UV-induced oxidation to a limited extent, providing only partial protection to the outermost polymer layer. For macro-to-microplastic conversion models, the following elements could be considered, where appropriate: (i) a biofilm-dependent crystallinity variable influencing brittleness; (ii) a cavity density variable, for example, informed by AFM roughness metrics (RMS, SSA); (iii) a moisture-related stress factor resulting from hydrated biofilms; and (iv) a UV-exposure variable coupled with a biofilm-attenuation factor to reflect partial shielding (i.e., a modest reduction in effective UV dose). Inclusion of such elements, may help reduce potential underestimation of biofilm-mediated fragmentation.

Taken together, these findings underscore the dual role of biofilms as both facilitator and mitigators of plastic degradation. Therefore, their dynamic interactions with plastic surface warrant explicit consideration in environmental aging studies. The exclusion of biofilm-plastic interactions from laboratory-based assessments likely underestimates the complexity and extent of plastic transformation under real-world conditions, potentially leading to an incomplete understanding of environmental microplastic behavior.

Future studies should include multiple exposure times to capture degradation kinetics and the temporal dynamics of biofilm-mediated plastic weathering. In addition, the longer-term consequences of biofilm activity on additive leaching warrant further investigation.

■ ASSOCIATED CONTENT

Data Availability Statement

The SI contains many additional information concerning sequencing, accelerated weathering and calculations of surface free energy. Measurement data from the AFM, μ-Raman, contact angles, and surface free energy are published in the open access data repository PANGAEA (pangaea.de).[34,35] Sequencing data is published in the European nucleotide archive with the accession number PRJEB90187.

Supporting Information

The Supporting Information is available free of charge at https://pubs.acs.org/doi/10.1021/acs.est.5c08345.

Pictures of PET in the four conditions; microbial community of the biofilm; 2D contour plots and 3D topography maps of the four PET conditions; Raman spectra of the Raman shift at 1097 and 1120 cm^{-1}; Raman spectra of the Raman shift at 1729 cm^{-1}; boxplots of height ratio between 1097 and 1120 cm^{-1} and $FHWM_{1729}$ for the different z-positions; and supplementary references (PDF)

■ AUTHOR INFORMATION

Corresponding Authors

Isabel Goßmann − *Department of the Built Environment, Aalborg University, 9220 Aalborg East, Denmark;* orcid.org/0000-0001-8848-4553; Email: isgo@build.aau.dk

Fan Liu − *Department of the Built Environment, Aalborg University, 9220 Aalborg East, Denmark;* orcid.org/0000-0002-7975-4790; Email: fl@build.aau.dk

Authors

Hery Mitsutake − *Department of the Built Environment, Aalborg University, 9220 Aalborg East, Denmark*

Julius Degenhardt − *Institute for Chemistry and Biology of the Marine Environment (ICBM), Carl von Ossietzky University of Oldenburg, 26111 Oldenburg, Germany*

Morten E. Simonsen − *Department of Chemistry and Bioscience, Aalborg University, 6700 Esbjerg, Denmark*

Complete contact information is available at: https://pubs.acs.org/10.1021/acs.est.5c08345

Funding

I.G.: Conceptualization, formal analysis, investigation, data curation, writing—original drift, visualization; H.M.: Formal analysis, investigation, data curation, writing—review & editing, visualization; J.D.: Formal analysis, investigation, resources, data curation, writing—review & editing, visualization; M.E.S.: Investigation, resources, data curation, writing—review & editing; F.L.: Conceptualization, resources, writing—review & editing, supervision, project administration, funding acquisition.

Notes

The authors declare no competing financial interest.

■ ACKNOWLEDGMENTS

This study was funded by the research grant from VILLUM FONDEN for the project *The neglected defender? Rethinking biofilms on plastic* (Villum Experiment, VIL58644; IG, FL). HM thanks the Novo Nordisk Fonden for financial support through the *OPTICS* project (grant number: 131970).

■ REFERENCES

(1) Jahnke, A.; Arp, H. P. H.; Escher, B. I.; Gewert, B.; Gorokhova, E.; Kühnel, D.; Ogonowski, M.; Potthoff, A.; Rummel, C.; Schmitt-Jansen, M.; Toorman, E.; MacLeod, M. Reducing Uncertainty and Confronting Ignorance about the Possible Impacts of Weathering Plastic in the Marine Environment. *Environ. Sci. Technol. Lett.* **2017**, *4* (3), 85−90.

(2) Liu, P.; Zhan, X.; Wu, X.; Li, J.; Wang, H.; Gao, S. Effect of Weathering on Environmental Behavior of Microplastics: Properties. *Sorption and Potential Risks. Chemosphere* **2020**, *242*, No. 125193.

(3) Schefer, R. B.; Armanious, A.; Mitrano, D. M. Eco-Corona Formation on Plastics: Adsorption of Dissolved Organic Matter to Pristine and Photochemically Weathered Polymer Surfaces. *Environ. Sci. Technol.* **2023**, *57* (39), 14707−14716.

(4) Ter Halle, A.; Ladirat, L.; Martignac, M.; Mingotaud, A. F.; Boyron, O.; Perez, E. To What Extent Are Microplastics from the Open Ocean Weathered? *Environ. Pollut.* **2017**, *227*, 167−174.

(5) Flemming, H.-C.; Wingender, J. The Biofilm Matrix. *Nat. Rev. Microbiol* **2010**, *8* (9), 623−633.

(6) *Periphyton: Ecology, Exploitation and Management*; Azim, M. E.; Verdegem, M. C. J.; Van Dam, A. A.; Beveridge, M. C. M., Eds.; CABI: Wallingford, 2005.

(7) Davey, M. E.; O'toole, G. A. Microbial Biofilms: From Ecology to Molecular Genetics. *Microbiol Mol. Biol. Rev.* **2000**, *64* (4), 847−867.

(8) Amaral-Zettler, L. A.; Zettler, E. R.; Mincer, T. J. Ecology of the Plastisphere. *Nat. Rev. Microbiol* **2020**, *18* (3), 139−151.

(9) Nauendorf, A.; Krause, S.; Bigalke, N. K.; Gorb, E. V.; Gorb, S. N.; Haeckel, M.; Wahl, M.; Treude, T. Microbial Colonization and Degradation of Polyethylene and Biodegradable Plastic Bags in Temperate Fine-Grained Organic-Rich Marine Sediments. *Mar. Pollut. Bull.* **2016**, *103* (1−2), 168−178.

(10) UNEP. *Single-Use Plastics, a Roadmap for Sustainability*; United Nations Environment Programme: Nairobi, Kenya, 2018.

(11) Simon, M.; Vianello, A.; Shashoua, Y.; Vollertsen, J. Accelerated Weathering Affects the Chemical and Physical Properties of Marine Antifouling Paint Microplastics and Their Identification by ATR-FTIR Spectroscopy. *Chemosphere* **2021**, *274*, No. 129749.

(12) Binnig, G.; Quate, C. F.; Gerber, Ch. Atomic Force Microscope. *Phys. Rev. Lett.* **1986**, *56* (9), 930−933.

(13) Butt, H.-J.; Cappella, B.; Kappl, M. Force Measurements with the Atomic Force Microscope: Technique, Interpretation and Applications. *Surf. Sci. Rep.* **2005**, *59* (1−6), 1−152.

(14) Ivleva, N. P. Chemical Analysis of Microplastics and Nanoplastics: Challenges, Advanced Methods, and Perspectives. *Chem. Rev.* **2021**, *121* (19), 11886−11936.

(15) Lohumi, S.; Kim, M. S.; Qin, J.; Cho, B.-K. Raman Imaging from Microscopy to Macroscopy: Quality and Safety Control of Biological Materials. *TrAC Trends in Analytical Chemistry* **2017**, *93*, 183−198.

(16) Perret, E.; Chen, K.; Braun, O.; Muff, R.; Hufenus, R. Radial Gradients in PET Monofilaments: A Raman Mapping and SAXS Tomography Study. *Polymer* **2022**, *238*, No. 124422.

(17) Primpke, S.; Booth, A. M.; Gerdts, G.; Gomiero, A.; Kögel, T.; Lusher, A.; Strand, J.; Scholz-Böttcher, B. M.; Galgani, F.; Provencher, J.; Aliani, S.; Patankar, S.; Vorkamp, K. Monitoring of Microplastic Pollution in the Arctic: Recent Developments in Polymer Identification, Quality Assurance and Control, and Data Reporting. *Arctic Science* **2023**, *9* (1), 176−197.

(18) *Confocal Raman Microscopy*; Toporski, J.; Dieing, T.; Hollricher, O., Eds.; Springer Series in Surface Sciences; Springer International Publishing: Cham, 2018; Vol. *66*.

(19) Fowkes, F. M. ATTRACTIVE FORCES AT INTERFACES. *Ind. Eng. Chem.* **1964**, *56* (12), 40−52.

(20) Marmur, A. Solid-Surface Characterization by Wetting. *Annu. Rev. Mater. Res.* **2009**, *39* (1), 473−489.

(21) Owens, D. K.; Wendt, R. C. Estimation of the Surface Free Energy of Polymers. *J. Appl. Polym. Sci.* **1969**, *13* (8), 1741−1747.

(22) Gewert, B.; Plassmann, M. M.; MacLeod, M. Pathways for Degradation of Plastic Polymers Floating in the Marine Environment. *Environ. Sci.: Processes Impacts* **2015**, *17* (9), 1513−1521.

(23) Degenhardt, J.; Dlugosch, L.; Ahrens, J.; Beck, M.; Waska, H.; Engelen, B. Seasonal Dynamics of Microbial Diversity at a Sandy High Energy Beach Reveal a Resilient Core Community. *Front. Mar. Sci.* **2020**, *7*, No. 573570.

(24) Francis, L. F.; Mccormick, A. V.; Vaessen, D. M.; Payne, J. A. Development and Measurement of Stress in Polymer Coatings. *J. Mater. Sci.* **2002**, *37*, 4717−4731.

(25) Jacques, S. L. History of Monte Carlo Modeling of Light Transport in Tissues Using Mcml.c. *Journal of Biomedical Optics* **2022**, *27* (8), No. 083002.

(26) Perret, E.; Braun, O.; Sharma, K.; Tritsch, S.; Muff, R.; Hufenus, R. High-Resolution 2D Raman Mapping of Mono- and Bicomponent Filament Cross-Sections. *Polymer* **2021**, *229*, No. 124011.

(27) Cui, X.-Y.; Ringer, S. P.; Wang, G.; Stachurski, Z. H. What Should the Density of Amorphous Solids Be? *J. Chem. Phys.* **2019**, *151* (19), 194506.

(28) Saharan, B. S.; Beniwal, N.; Duhan, J. S. From Formulation to Function: A Detailed Review of Microbial Biofilms and Their Polymer-Based Extracellular Substances. *Microbe* **2024**, *5*, No. 100194.

(29) Legras, R.; Bailly, C.; Daumerie, M.; Dekoninck, J. M.; Mercier, J. P.; Zichyt, M. V.; Nield, E. Chemical Nucleation, a New Concept Applied to the Mechanism of Action of Organic Acid Salts on the Crystallization of Polyethylene Terephthalate and bisphenoI-A Polycarbonate. *Polymer* **1984**, *25*, 835−844.

(30) Di Lorenzo, M. L. Crystallization of Poly(Ethylene Terephthalate): A Review. *Polymers* **2024**, *16* (14), No. 1975.

(31) Zhang, J.; Wang, X.; Gong, J.; Gu, Z. A Study on the Biodegradability of Polyethylene Terephthalate Fiber and Diethylene Glycol Terephthalate. *J. Appl. Polym. Sci.* **2004**, *93* (3), 1089−1096.

(32) Patnaik, P. *Dean's Analytical Chemistry Handbook*, 2nd ed.; McGraw-Hill handbooks; McGraw-Hill: New York, 2004.

(33) Delorme, A. E.; Lebreton, L.; Royer, S.-J.; Kāne, K.; Arhant, M.; Le Gall, M.; Le Gac, P.-Y. Assessing Plastic Brittleness to Understand Secondary Microplastic Formation on Beaches: A Hotspot for Weathered Marine Plastics. *Microplast. Nanoplast.* **2025**, *5* (1), 25.

(34) Felden, J.; Möller, L.; Schindler, U.; Huber, R.; Schumacher, S.; Koppe, R.; Diepenbroek, M.; Glöckner, F. O. PANGAEA - Data Publisher for Earth & Environmental Science. *Sci. Data* **2023**, *10* (1), 347.

(35) Goßmann, I.; Mitsutake, H.; Degenhardt, J.; Simonsen, M. E.; Liu, F. Measurements of Polyethylene Terephthalate Surface Changes after UV Exposure and Biofilm Growth. *PANGAEA* **2025**, DOI: 10.1594/PANGAEA.984585.